Journal of *Marine Science and Engineering*

MDPI

Article

Interconnection between the Southern South China Sea and the Java Sea through the Karimata Strait

Poh Heng Kok [1], Sarath Wijeratne [2], Mohd Fadzil Akhir [1,*], Charitha Pattiaratchi [2], Nur Hidayah Roseli [1,3] and Fariz Syafiq Mohamad Ali [1]

[1] Institute of Oceanography and Environment, Universiti Malaysia Terengganu, Kuala Nerus 21030, Terengganu, Malaysia; pohhengkok@umt.edu.my (P.H.K.); nurhidayahroseli@umt.edu.my (N.H.R.); farizsyafiq10@gmail.com (F.S.M.A.)
[2] Ocean Graduate School, The UWA Ocean Institute, The University of Western Australia, Crawley, WA 6009, Australia; sarath.wijeratne@uwa.edu.au (S.W.); chari.pattiaratchi@uwa.edu.au (C.P.)
[3] Faculty of Science and Marine Environment, Universiti Malaysia Terengganu, Kuala Nerus 21030, Terengganu, Malaysia
* Correspondence: mfadzil@umt.edu.my

Abstract: This study aims to investigate the interconnection between the southern South China Sea (SSCS) and Java Sea (JS) by simulating seasonal circulations and associated transports using the Regional Ocean Modelling System (ROMS). The seasonal circulation was predominantly driven by monsoonal wind stress and water exchanges between the SSCS and the JS. During the boreal winter, cooler and saltier waters from the SSCS were advected into the JS, while during the boreal summer, cooler waters from the JS were advected into the SSCS, with the advection of fresher water onto the Peninsular Malaysia's east coast in the SSCS being the new finding provided by this study. The various water transports were driven southward into the JS during the boreal winter and northward into the SSCS during the boreal summer. The various water transports estimated by ROMS peaked in May during the inflow months from the JS into the SSCS, which was attributed to the simulated anticyclonic eddy in the SSCS, which differed from previous studies that peaked between June and August. The annual mean volume, freshwater, heat, and salt transports were 0.96 Sv, 0.04 Sv, 0.10 PW, and 0.03 $\times$ 10^9 kg s^{-1}, respectively, directed from the SSCS into the JS.

Keywords: Regional Ocean Modelling System; South China Sea; Java Sea; water transports

Citation: Kok, P.H.; Wijeratne, S.; Akhir, M.F.; Pattiaratchi, C.; Roseli, N.H.; Mohamad Ali, F.S. Interconnection between the Southern South China Sea and the Java Sea through the Karimata Strait. *J. Mar. Sci. Eng.* **2021**, *9*, 1040. https://doi.org/10.3390/jmse9101040

Academic Editor: Anatoly Gusev

Received: 10 July 2021
Accepted: 4 September 2021
Published: 22 September 2021

1. Introduction

The southern South China Sea (SSCS) and the Java Sea (JS) are water bodies of the Southeast Asia Maritime Continent, located at the confluence of the tropical Pacific and Indian Oceans (Figure 1). The South China Sea (SCS) is one of the largest marginal seas in the western Pacific, positioned between 0–25° N and 99–122° E with an average depth of approximately 2000 m. The SCS is influenced by the East Asian monsoon [1,2]. In the boreal summer, the SCS is influenced by the southwest monsoon, where the southwesterly wind prevails over the SCS, while in the boreal winter, the SCS is influenced by the northeast monsoon, where the northeasterly wind prevails over the SCS [3,4]. The SSCS is connected to the JS via the shallow Karimata Strait, with a sill depth of about 45 m. The JS is located between 2.5–8.5° S and 105.5–120.5° E, with an average depth of about 40 m. The JS is affected by the Asian–Australian monsoon system, known as the southeast and northwest monsoons. During the southeast monsoon, the southeasterly wind prevails over the JS throughout the boreal summer, while during the northwest monsoon, the winds are reversed to the northwesterly and prevail throughout the boreal winter [5,6].

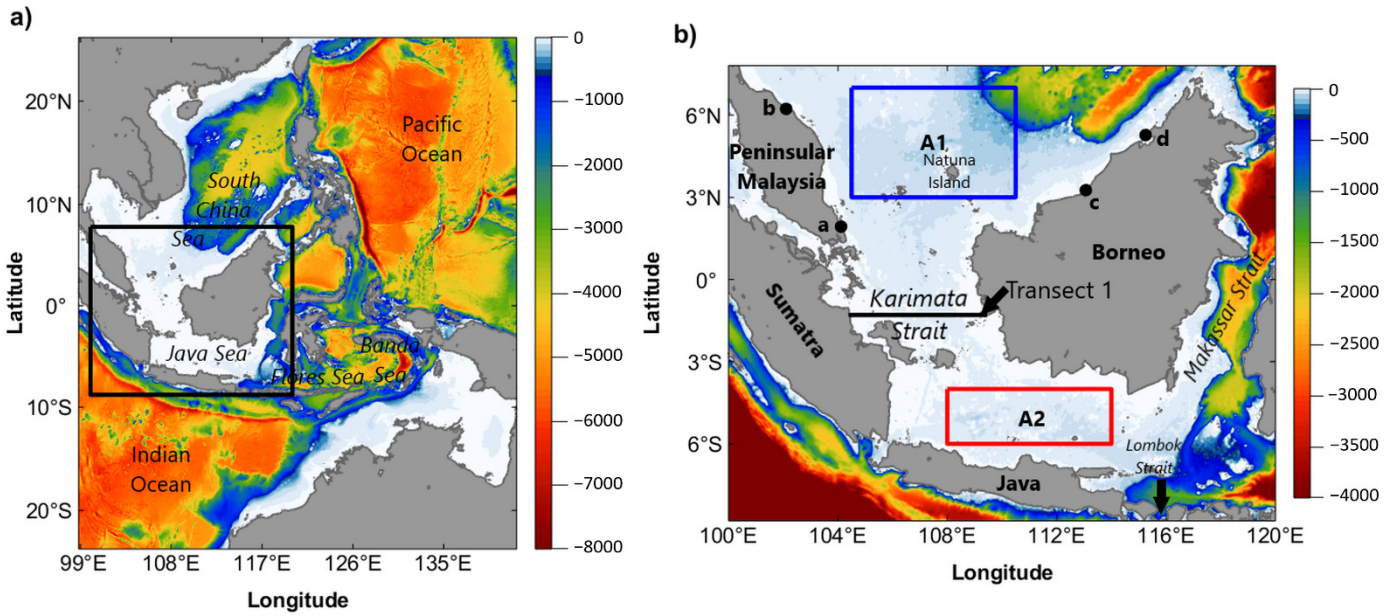

Figure 1. Model domain and bathymetry (unit: m). Black box in (**a**) represent the region of interest as shown in (**b**). Blue and red boxes in (**b**) represent the domains of the SSCS (A1) and the JS (A2). Black line in (**b**) is the transect (Transect 1) used to estimate various Karimata Strait transports (KSTs). Black dots in (**b**) mark the location of four tide gauge stations: (a) Tanjung Selidi, (b) Getting, (c) Bintulu, and (d) Labuan, used to validate the mean sea levels.

The surface circulation of the SSCS and the JS is predominately influenced by the monsoon winds. The surface circulation in the SSCS is directed southward during the boreal winter, and northward during the boreal summer [2,7]. In addition, many studies have revealed that the general circulation of the SSCS is cyclonic during the boreal winter and anticyclonic during the boreal summer [8–13]. In the JS, the prevailing winds drive the surface circulation eastward during the boreal winter and westward during the boreal summer [5,14]. In the SSCS, the strong wind stress during the boreal winter introduces cooler and denser waters into the mixed layer, resulting in a cooler sea surface temperature (SST), whereas the decline in wind stress and the trapping of heat in the mixed layer resulted in an increase of SST during the boreal summer [15]. The seasonal variation of SST in the JS is relatively small in comparison with the SSCS; however, the sea surface salinity (SSS) in the JS is subject to a wide range of variation depending on the seasonal movement of water mass from adjacent seas. The monsoon wind engulfs fresher water from the SCS into the JS in boreal winter, while the monsoon wind in the boreal summer shifts saltier water from the eastern part of the JS into the JS, resulting in lower and higher SSS, respectively [5,16].

There is an important mean circulation system between the SSCS and the JS, which is the existence of the Karimata Strait throughflow (KSTF). The KSTF is characterized as the efflux seepage of the South China Sea throughflow (SCSTF) and a branch of the Indonesian throughflow (ITF). The KSTF is notable for transporting buoyant and fresher waters from the SCS into the Makassar Strait, resulting in a northward pressure gradient that restricts the ITF from transporting surface Pacific waters southward into the Indian Ocean [17–20]. Although the strength of the KSTF is weaker than the ITF by about half an order, it plays a significant role in maintaining the heat and salt balance of the SCS [17]. The strength of the KSTF is determined by estimating the Karimata Strait transport (KST). The estimation of the KST has been subjected to many investigations. Based on field measurements, Wyrtki [2], Fang et al. [21], and Susanto et al. [22] estimated that various KSTs (volume, heat, freshwater, and salt transports) are directed southward from the SSCS towards the JS with stronger intensity during the boreal winter, and in the opposite direction during the boreal summer with weaker intensity. In recent years, several ocean models have been conducted to estimate various KSTs on either a seasonal [8,23] or annual

timescale [13,24–26]. Nevertheless, the estimated various transports are fraught with significant uncertainty, owning to differences in model configurations and resolutions, particularly when the shallow areas and pathways are linked to the channels and adjacent seas [27].

Even though the SSCS and the JS are interconnected, most of the cited studies focus on surface circulation in the SSCS and the JS separately; thus, comprehensive knowledge of the interconnection between these two water bodies and the associated various transports through the Karimata Strait remains ambiguous. Furthermore, the bathymetry and circulation patterns between the SSCS and the JS are complex, and observational data in this region are sparse; thus, a higher resolution ocean model, as proposed by this study, is required for a better understanding of the interconnection between these water bodies and a better estimation of various transports.

According to the above assertions, the objectives of this study are specified to investigate the seasonal interconnection between the SCS and the JS, as well as the related dynamics of various transports through the Karimata Strait using a finer resolution ocean model. The rest of this paper is organized as follows. Section 2 describes the data and methods employed in this study, while Section 3 contains the results and discussion of the physical characteristics between the SCS and the JS through the Karimata Strait as well as the various KSTs. Section 4 presents the summary and conclusion.

2. Data and Methods

2.1. Model Description and Configuration

This study employed a free-surface, split-explicit, and terrain-following coordinate regional ocean model, i.e., Regional Ocean Modelling System (ROMS) [28], developed collaboratively by Rutgers University, University of California Los Angeles, and worldwide researchers, https://www.myroms.org/, accessed on 8 September 2021 [29].

The model domain encompassed between 23.65° S–25.97° N and 98.82° E–142.22° E (Figure 1a), with a horizontal resolution of 5–6 km (960 × 960 grid points), to include as many topographical details as possible and to resolve the major mesoscale eddy structures. The bathymetry data were derived from the General Bathymetric Chart of the Oceans (GEBCO) 15 arc-second gridded bathymetric data, https://www.gebco.net/data_and_products/gridded_bathymetry_data/gebco_2019/gebco_2019_info.html, accessed on 8 September 2021, GEBCO_2019 [30]. The model consisted of 30 vertical s-levels with the grid stretching and transformation parameters selected to establish a higher resolution towards the surface and bottom boundaries, allowing the ocean boundary layers to be better resolved. The bathymetry was smoothed to reduce horizontal pressure gradient errors according to the following steps: (1) the bathymetry was smoothed using a Gaussian filter with a width twice the size of each data point; (2) smoothing was performed at depths below 4500 m over the entire computational grid; (3) all spikes with depths above 4500 m were smoothed; and (4) the model domain was separated into different sub-regions and the bathymetry in each of the sub-regions was smoothed using a smooth positive method [31].

Surface wind stress, sea level pressure, heat, and freshwater fluxes with a horizontal resolution of 0.25° × 0.25° for the atmospheric forcing parameter were acquired from the hourly European Center Medium-Range Weather Forecast (ECMWF) fifth generation atmospheric reanalysis (ERA5), https://www.ecmwf.int/en/forecasts/datasets/reanalysis-datasets/era5, accessed on 8 September 2021 [32].

The present ocean model was nested within the global ocean model, i.e., Hybrid Coordinate Ocean Model (HyCOM) + Navy Coupled Ocean Data Assimilation (NCODA) Global 1/12° Analysis (GLBu0.08) (hereafter referred to as HyCOM), which is forced by the National Centers for Environmental Prediction (NCEP) Climate Forecast System Reanalysis (CFSR). Observation data are assimilated into the HyCOM by means of the Navy Coupled Ocean Data Assimilation (NCODA) system [33,34]. NCODA incorporates the model forecast as a first guess in a 3D variation scheme, then satellite altimeter, satellite-derived and in situ SST, and in situ temperature and salinity vertical profiles are subsequently

assimilated into the model. Modular Ocean Data Assimilation System (MODAS) synthetics are used to project surface information downward [35]. Further details of HyCOM data can be found at https://www.hycom.org/, accessed on 8 September 2021.

The identical model boundary setup and parameters were utilized by Wijeratne et al. [36]. Mean sea levels, salinity, temperature, and transport (barotropic and 3D velocity components) obtained from HyCOM were prescribed as open boundary conditions. For the baroclinic mode (temperature, salinity, and baroclinic momentum), a combination of Orlanski-type radiation boundary conditions with nudging was used [37]. The nudging band is the same dimension as the sponge layer, which comprises nine grid cells (~46 km). Within the sponge layer, nudging was used to relax the temperature and salinity to the ROMS solutions on a daily time scale.

A total of 13 tidal constituents with a resolution of 0.25°, including eight primary (M2, S2, N2, K2, K1, O1, P1, Q1), three non-linear (M4, MS4, MN4), and two long periods (Mf and Mm), were acquired from the Oregon State University TOPEX/Poseidon Global Inverse Solution (TPXO) version 7.2 global tidal model [38], http://g.hyyb.org/archive/Tide/TPXO/TPXO_WEB/global.html, accessed on 8 September 2021. These tidal constituents were relaxed at the open boundaries using the Flather condition [39] for depth-averaged current ellipses and the Chapman condition [40] for elevation. These schemes allow prescribed tidal disturbances to enter the model domain, while also allowing tidal disturbances to leave the domain seamlessly.

The model was run in hindcast mode with an absence of data assimilation from 1 January 2001 to 31 December 2015 (15 years). The model was initialized with HyCOM data and pre-run for 1 year (January–December 2000) for model spin-up. The simulated surface temperature data were relaxed to a daily surface field derived from HyCOM for correcting atmospheric heat fluxes to prevent significant SST drift [41–43]. Furthermore, simulated surface salinity data were relaxed to a daily surface field derived from HyCOM to prevent significant SSS drift due to insufficient precipitation minus evaporation forcing [44]. The relaxation of SSS into the model has been shown to result in a more realistic spatial distribution of salinity in the model [45], whereas the relaxation of both SST and SSS into the model can ensure the right water masses are formed at the right density, with subsequent circulation, subduction, and deep convection further transporting them at depth [46].

The region of interest occupied the area between the SSCS and the JS (Figure 1b), with the goal of examining the interconnection between these two water bodies and the associated various transports through the Karimata Strait. Unless otherwise specified, all the results examined were based on climatological data.

2.2. Analytical Techniques

2.2.1. Model Validation

It should be noticed that the sea surface height was not relaxed in the present ocean model; therefore, the estimated mean sea levels could be validated against the observed mean sea levels. This was accomplished by validating the estimated mean sea levels against the observed mean sea levels acquired from the Permanent Service for Mean Sea Levels (PSMSL), https://www.psmsl.org/, accessed on 8 September 2021 [47] at four tide gauge stations located in the southern SCS (black dots in Figure 1b).

In addition, the simulated surface current, SST, and SSS were mainly validated against the Copernicus Marine Environment Monitoring Service (CMEMS) global reanalysis product, i.e., GLOBAL_REANALYSIS_PHY_001_030, https://resources.marine.copernicus.eu/?option=com_csw&view=details&product_id=GLOBAL_REANALYSIS_PHY_001_030, accessed 8 on September 2021. This CMEMS model is a 1/12° eddy resolving global ocean model based on the Nucleus for Modelling of the Ocean (NEMO) ocean model, which is driven by the ECMWF Interim Reanalysis (ERA-Interim) and then ERA5 from 1 January 2019. The along-track altimeter (sea level anomaly), satellite-derived SST, sea ice concentration, and in situ temperature and salinity vertical profiles are assimilated into the model using a reduced-order Kalman filter. Furthermore, slowly evolving large-scale temperature

and salinity biases are corrected using a 3D-VAR scheme [48]. This model has undergone a quality assessment and has been shown to be appropriate for representing oceanographic variables [49,50].

As previously stated, the SST and SSS of the present ocean model were relaxed to daily surface temperature and salinity derived from HyCOM; thus, to determine the exact reliability of the simulation, the temperature and salinity at 5 m derived from the present ocean model were treated as SST and SSS, respectively, as such for the CMEMS. In addition, 4 km × 4 km horizontal resolution of satellite-derived SST obtained from the Moderate Resolution Imaging Spectroradiometer (MODIS) on board the Aqua satellite was used as an additional data source for SST validation, https://oceancolor.gsfc.nasa.gov/, accessed on 8 September 2021 [51]. Moreover, the simulated SSS was compared to World Ocean Atlas (WOA) 2018 data with a horizontal resolution of 0.25°, which are freely available, uniformly formatted, and quality monitored, https://www.ncei.noaa.gov/products/world-ocean-atlas, accessed on 8 September 2021 [52].

2.2.2. Wind Stress and Wind Stress Curl

The seasonal zonal and meridional wind speed vectors at 10 m with a horizontal resolution of 0.25° × 0.25° were obtained from ERA5 [32] to compute wind stress and wind stress curl within the study region. The zonal (τ_x) and meridional (τ_y) components of wind stress were defined as follows:

$$\tau_x = \rho_a C_d W_{mag} U \quad (1)$$

$$\tau_y = \rho_a C_d W_{mag} V \quad (2)$$

where ρ_a is the density of air; C_d is the dimensionless drag coefficient; W_{mag} is the wind magnitude; and U and V are the zonal and meridional wind speed components, respectively. The corresponding wind stress curl ($curl(\tau)$) was calculated as follows:

$$curl(\tau) = \frac{\partial \tau_y}{\partial_x} - \frac{\partial \tau_x}{\partial_y} \quad (3)$$

2.2.3. Water Transports

To estimate the water transports through the Karimata Strait, i.e., KSTs, a transect line lie between east Sumatra and west Borneo at a latitude of 1.3° S, named as Transect 1 in Figure 1b, was designated. The full-depth volume transport (F_V) across Transect 1 was calculated by the following equation, adapted from Fang et al. [21]:

$$F_V = \int_A v dA \quad (4)$$

where v is the meridional velocity component and dA is the area element of Transect 1. The calculated volume transport was multiplied by the normal vector perpendicular to Transect 1. Henceforward, positive values denoted outflow through the Karimata Strait into the JS, whereas negative values denoted inflow through the Karimata Strait into the SSCS. According to Fang et al. [21], freshwater transport (F_W) was computed using the following equation:

$$F_W = \int_A [(S_0 - S)/S_0] v dA \quad (5)$$

where S is the salinity and S_0 is the reference salinity taken as 34.62 psu based on Levitus and Boyer [53]. For the heat transport (F_H), the following equation adapted from Fang et al. [21] was used:

$$F_H = pC_p \int_A (T - T_0) v dA \quad (6)$$

where p is the water density, taken as 1021 kg m^{-3} for a mean temperature of 28 °C and a mean salinity of 33 psu. C_p is the specific heat, T is the temperature, and T_0 is the reference temperature taken as 3.72 °C according to Ffield et al. [54] and Schiller et al. [55]. pC_p was

regarded as the heat capacity per unit volume, taken as 4.1×10^6 J m^{-3} K^{-1} for the stated mean temperature and mean salinity. Salt transport (F_S) was obtained by the following equation, adapted from Fang et al. [21]:

$$F_S = p \int_A SvdA \quad (7)$$

3. Results and Discussion

3.1. Wind Stress and Wind Stress Curl

During the boreal winter (December–January–February; DJF), northeasterly wind stress prevailed over the SSCS (Figure 2a). The wind stress intensity gradually declined and changed direction as it passed over the Karimata Strait and the JS, becoming northwesterly. During the boreal summer (June–July–August; JJA), wind stress reversed, with stronger southeasterly wind stress dominating over the JS and Karimata Strait, while weaker southwesterly wind stress prevailed over the SSCS (Figure 2b).

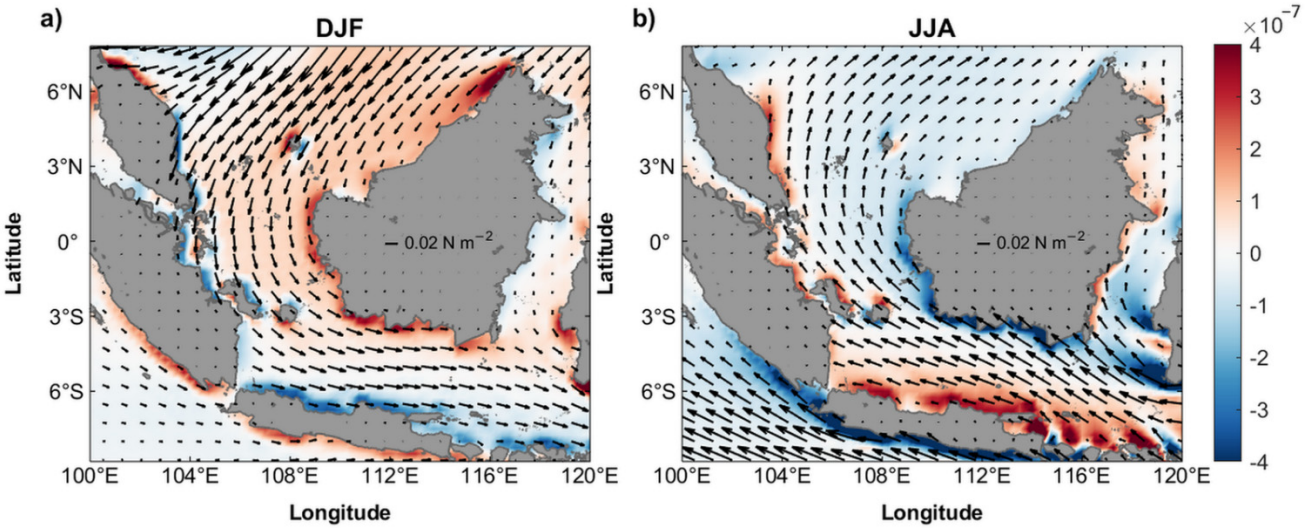

Figure 2. Seasonal wind stress vector (unit: N m^{-2}) and wind stress curl (unit: N m^{-3}; in shade) climatology during the (**a**) boreal winter and (**b**) boreal summer.

In general, the sign of wind stress curl during the boreal winter and boreal summer for the entire domain was in the opposite. A major part of the SSCS and Karimata Strait was dominated by positive wind stress curl during the boreal winter and negative during the boreal summer. Despite this, negative and positive wind stress curl was perceived along the Peninsular Malaysia's east coast (PMEC) during the boreal winter and boreal summer, respectively. The prevalence of positive wind stress curl endangers surface divergence, which has been shown to trigger upwelling along the PMEC during the boreal summer [56–60].

Dissimilar to the SSCS and Karimata Strait, the wind stress curl in the JS was typically asymmetric in both seasons. During the boreal winter, the northern JS was subjected to positive wind stress curl, whereas the southern JS was subjected to negative wind stress curl. During the boreal summer, the wind stress curl turned into negative in the northern JS and positive in the southern JS. Nonetheless, apart from the coastal area, the intensity of these wind stress curls in the JS was typically weaker than in the SSCS.

The positive wind stress curl corresponds to cyclonic circulation in the Northern Hemisphere, but anticyclonic circulation in the Southern Hemisphere. In contrast, negative wind stress curl corresponds to anticyclonic circulation in the Northern Hemisphere, but cyclonic circulation in the Southern Hemisphere [61–63]. Hence, the prevailing winds are known to alter surface circulation, especially at latitudes between 5° N and 5° S, where the Coriolis force is insignificant [13], which will be discussed in the subsequent section.

3.2. Meal Sea Levels

Figure 3 depicts a comparison of monthly mean sea levels derived from ROMS and PSMSL. It can be revealed that the estimated monthly mean sea levels closely resemble the observed data, exhibiting a comparable trend and amplitude at all four stations. The root mean square error (RMSE) of monthly mean sea levels between the present ocean model and observed data was less than or equal to 0.08 at all stations, suggesting that the present ocean model predicted mean sea levels reasonably well. The monthly mean sea levels at all stations exhibited seasonal fluctuation, with a single peak and trough throughout the boreal winter and summer, respectively. This annual cycle is typically caused by the seasonal reversal of monsoon winds. During the boreal winter, the northeast monsoon wind creates a sea level surge in the SSCS, whereas during the boreal summer, the southwest monsoon wind pushes water from the SSCS to the northwest part of the SCS, resulting in a fall in sea level [64].

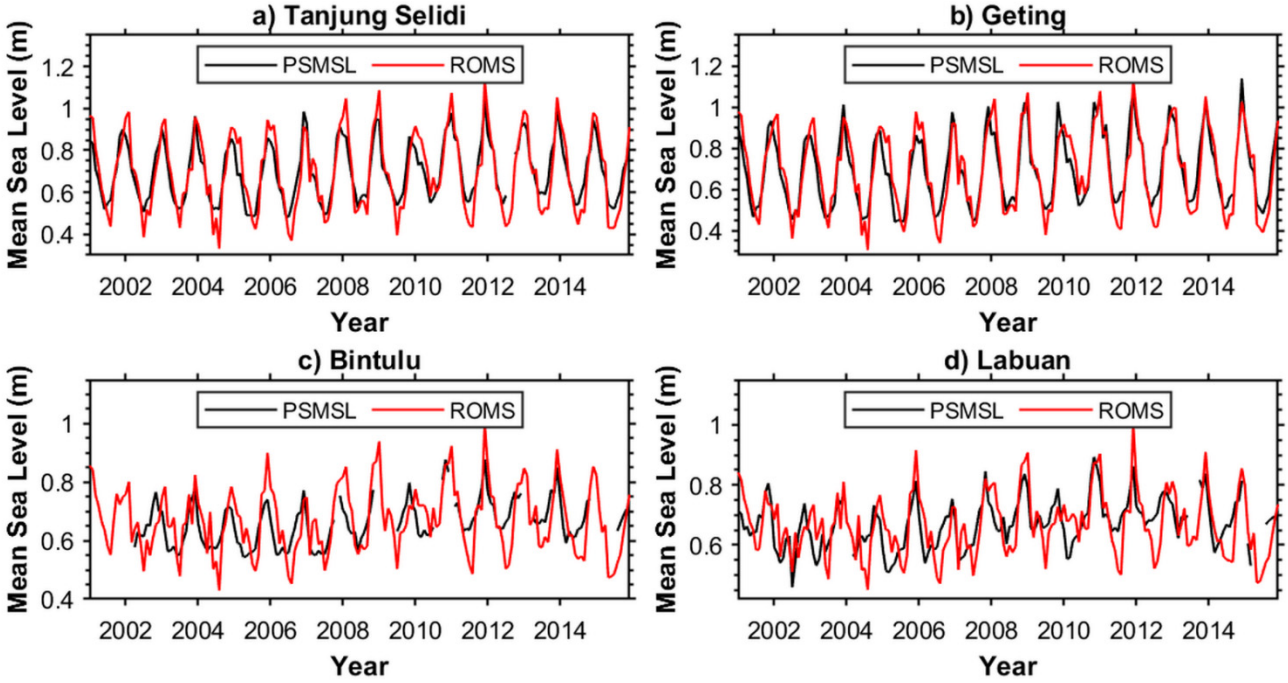

Figure 3. Monthly mean sea levels (unit: m) derived from PSMSL (black lines) and ROMS (red lines) at (**a**) Tanjung Selidi, (**b**) Geting, (**c**) Bintulu, and (**d**) Labuan.

Even though the ROMS mean sea levels showed some similar patterns and the RMSEs between both models and PSMSL were appropriate, the ROMS model appeared to overestimate the peak and trough. Potential explanations for this discrepancy include lower resolution of ERA5 ($0.25^\circ \times 0.25^\circ$) meteorological forcing and their bias in wind estimation. According to Minola et al. [65], ERA5 has a tendency to overestimate wind speeds, particularly in coastal areas. Based on an analysis of ERA5 data in the SCS, Jiang et al. [66] found that the wind speed was significantly overestimated, the zonal component was commonly underestimated, and the meridional component was significantly overestimated. In addition, a study of multiplatform wind products in the SCS throughout the boreal summer and autumn of 2019 revealed the RMSEs of ERA5 wind speed and wind direction were around 1.9 m s^{-1} and 33°, respectively [67]. In addition, there is a slight difference in the location because the tide gauges are positioned in an inner estuary/harbor with a shallow water depth, but the minimum model bathymetry is 4 m. It should also be noted that the predicted mean sea levels were not assimilated; thus, variations between observed and predicted mean sea levels are expected.

3.3. Surface Current

The simulated surface current was in general agreement with those derived from CMEMS and earlier findings by Fang et al. [27], He et al. [23], and Wyrtki [2,68] (Figure 4). ROMS and CMEMS revealed the existence of a quasi-surface current and an eddy structure situated in the SSCS, which is consistent with the findings by Fang et al. [27] and He et al. [23]. Generally, surface current in the SSCS and the JS was driven by wind stress, reflecting seasonal monsoon variability.

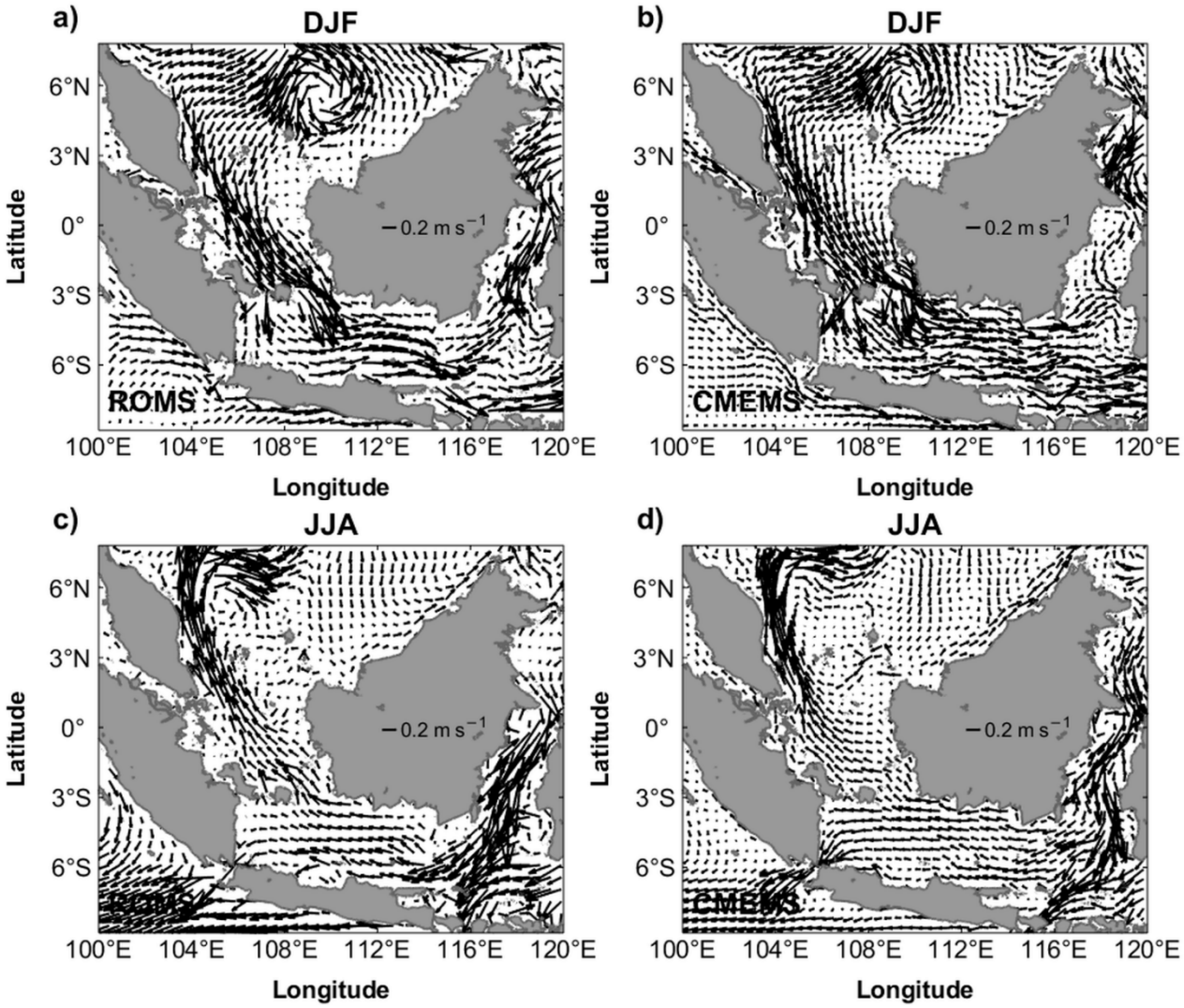

Figure 4. Seasonal surface current (unit: m s^{-1}) climatology during the (**a**,**b**) boreal winter and (**c**,**d**) boreal summer derived from ROMS (**left** panel) and CMEMS (**right** panel).

During the boreal winter, the distinct current laid along the PMEC (Figure 4a,b). The northeasterly monsoon winds during the boreal winter pushed the surface current along the PMEC southward. This western boundary current continued to flow southward across the Karimata Strait before turning eastward and merging with the eastward surface current driven by the northwesterly monsoon winds in the JS. This eastward surface current bifurcated in the eastern JS, with a portion continuing eastward into the Flores Sea. Meanwhile, a portion of it veered north and met the southward flowing current in the southern Makassar Strait. This northward flowing current in the Makassar Strait significantly reduces the strength of ITF, resulting in the weakest ITF outflow during the boreal winter [69]. Previous findings indicated that the monsoon wind drives surface

current eastward, pushing buoyant surface water from the SCS and the JS into the Flores and Banda Seas, with water piling up in the southern Makassar Strait because of the cramped exit. This situation raises the sea surface height and creates a pressure gradient, substantially reducing the strength of the southward flowing current in the Makassar Strait [18,20,69–71]. In addition, a cyclonic eddy was resembled in SSCS by the simulated model; CMEMS; and previous findings by Akhir [9], Chu et al. [72], Daryabor et al. [73], and Tangang et al. [10], centered at about 110° E, incarnating the associated positive wind stress curl. Nonetheless, the cyclonic eddy captured by CMEMS was weaker than ROMS, which was probably owing to the differing atmospheric forcing parameters employed by CMEMS, which used ERA-Interim, whereas the present ocean model used ERA5 during the simulation period.

During the boreal summer, the surface current reflected the variations as the monsoon wind reversed (Figure 4c,d). In the Makassar Strait, a strong current flowed southward and divided in the southern part of the strait, with the bulk of the surface current continuing to flow southward and drifting through the Lombok Strait—the main exit passages of the ITF [18,74,75]. During this season, the reversing monsoon wind drives surface water from Banda and Flores Seas westward, wipes off the northward pressure gradient, and allows unrestricted surface current to flow southward along the Makassar Strait [18,20]. Despite this, a portion of the southward surface current from the Makassar Strait shifted westward and joined the westward surface current in the JS, which was expelled by the southeasterly monsoon wind. Under the influence of southeasterly monsoon winds, this surface current in the Karimata Strait shifted north, joining the strong western boundary current along the PMEC.

There was a difference in the surface current circulation pattern between ROMS and CMEMS during the boreal summer. As shown in ROMS in the region north of the PMEC, the intense western boundary current generated unstable meandering when reaching the Gulf of Thailand and the adjacent coasts. These meandering currents became more intense and whirling, forming a clockwise motion at the northeast of PMEC. This anticyclonic eddy caused some of the western boundary current deflected eastward at the northwest of Natuna Island. The eastward movement of the deflection current meandered southwestward, swirled, and met the western boundary current system, generating another anticyclonic eddy with weaker intensity at the southwest of Natuna Island (southern part of the PMEC). This was particularly apparent in Supplementary Figure S1, which demonstrated the surface current derived from ROMS in June, July, and August. The circular pattern of this eddy was more obvious in June and decreased in size in July and August. Nevertheless, the existence of dual anticyclonic structures off the PMEC during the boreal summer was not represented in CMEMS, which could be attributed to the slightly coarser resolution of CMEMS. In addition, it differed from previous findings by Akhir [9] and Tangang et al. [10], which only simulated a single anticyclonic eddy somewhat bigger in size in the vicinity of the Natuna Island, which could be owing to the differing ocean model configuration utilized. Although the dual anticyclonic eddies were successfully simulated by Daryabor et al. [58], further investigation is needed to prove their occurrence, particularly through field observations. The existence of these eddies must be confirmed because they are a source of kinetic energy that convey momentum and trace water characteristics vertically and horizontally [76]. Through vertically mixing in and around the eddies, they play a critical role in pelagic ecosystem, biogeochemical cycles, and distribution of phytoplankton [77–79]. Furthermore, the prevalence of these eddies is regarded to be crucial off the PMEC and are influenced by upwelling processes because they often drive nutrient-rich coastal upwelling water offshore, which supports biological activity in the offshore region [80].

3.4. Sea Surface Temperature and Salinity

As previously stated, the SSCS and the JS are in the monsoon regime. Consequently, the water characteristics in this region undergo seasonal changes. The model simulated SST

(Figure 5) and SSS (Figure 6) were generally compatible with those derived from CMEMS, MODIS, or WOA. However, the simulated model appeared to be cooler than MODIS and CMEMS during both seasons. The SST bias between CMEMS and ROMS in the study domain was 0.10 °C during the boreal winter and 0.31 °C during the boreal summer, while the bias between MODIS and the simulated model was 0.07 °C during the boreal winter and 0.43 °C during the boreal summer. In terms of SSS, the simulated model appeared to have a higher SSS than CMEMS and WOA in the study domain. The SSS bias between CMEMS and ROMS was 0.79 psu during the boreal winter and 0.60 psu during the boreal summer, whereas the bias between WOA and ROMS was 0.45 psu during the boreal winter and 0.36 psu during the boreal summer.

The presence of bias in SST and SSS could be attributed to several factors, such as the different atmospheric forcing parameters used in the model that interact with the topography and bathymetry at each grid point, as well as different model configurations. Additionally, the horizontal and vertical resolutions of the model, as well as the characteristic turbulent diffusion times attributable to vertical turbulent diffusion and vertical advection or convection of the layer, also may be factors [81].

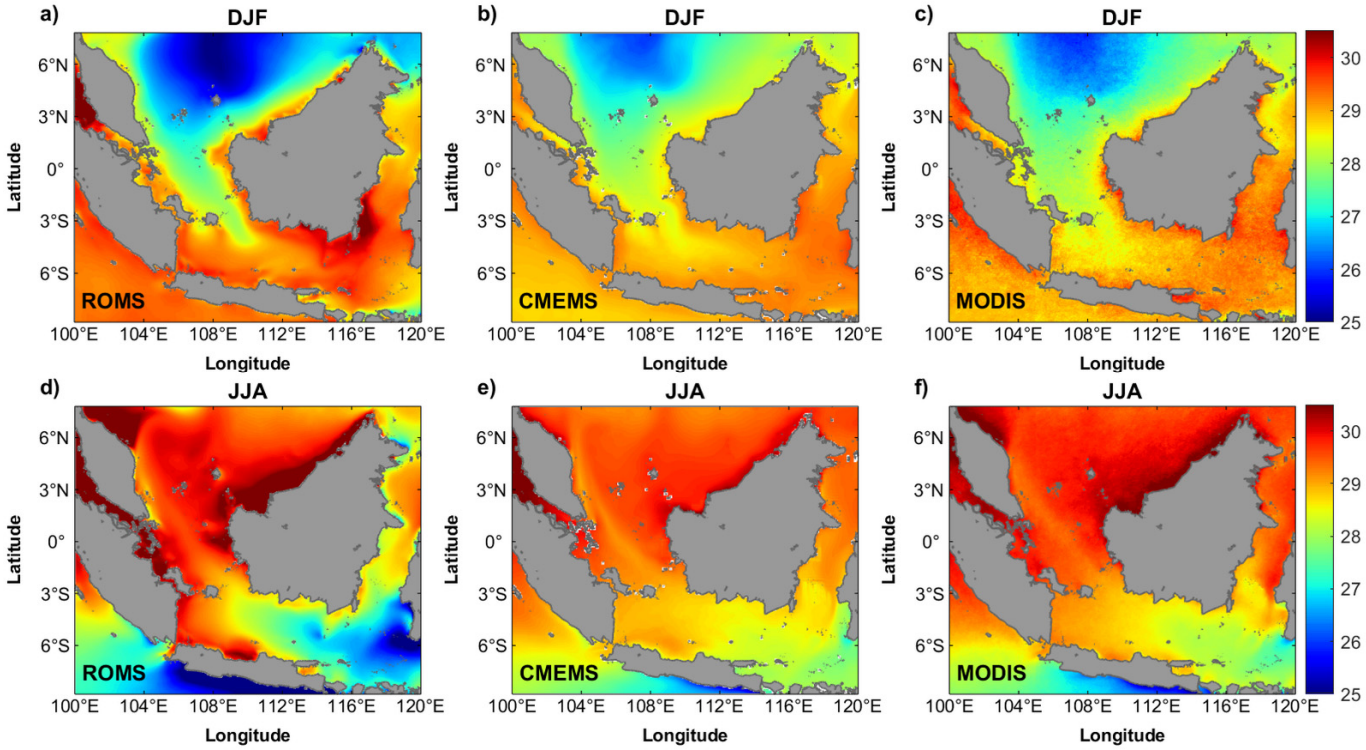

Figure 5. Seasonal SST (unit: °C) climatology during the (**a**–**c**) boreal winter and (**d**–**f**) boreal summer derived from ROMS (**left** panel), CMEMS (**middle** panel), and MODIS (**right** panel).

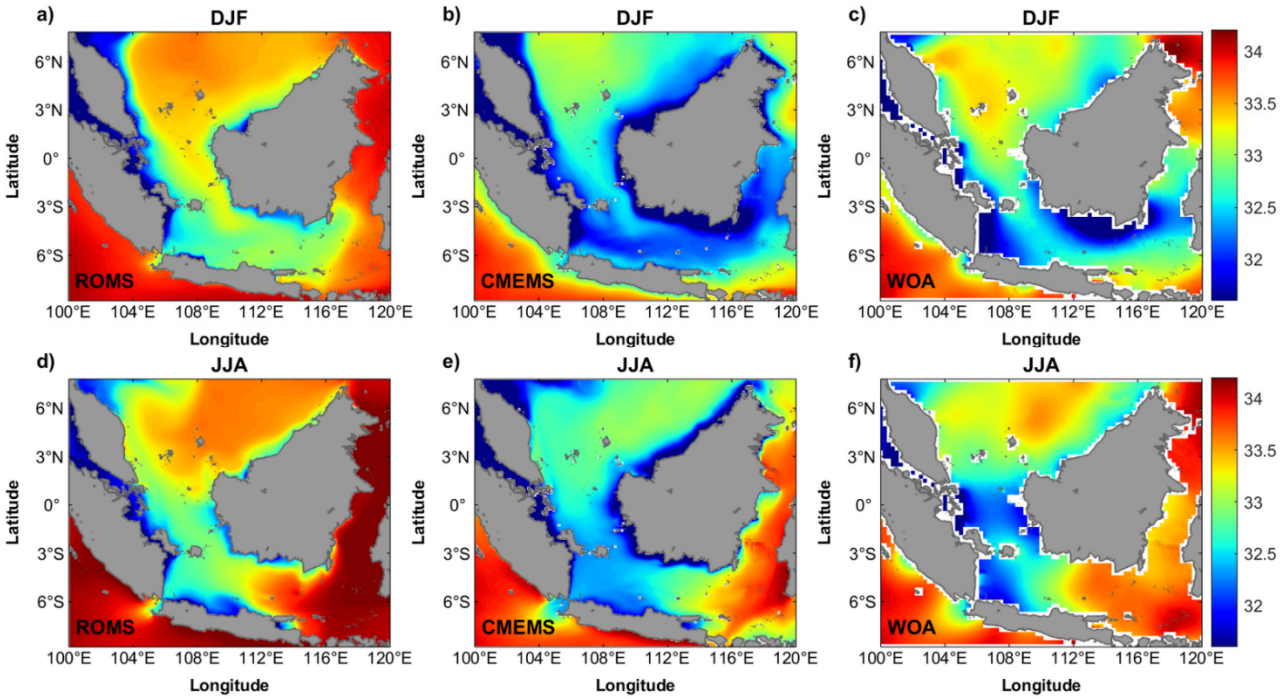

Figure 6. Seasonal SSS (unit: psu) climatology during the boreal winter (**a**–**c**) and boreal summer (**d**–**f**) derived from ROMS (**left** panel), CMEMS (**middle** panel), and WOA (**right** panel).

As observed from the SST (Figure 5) and SSS (Figure 6) maps, the distributions of SST and SSS in the SSCS and JS were not identical; they were cooler and saltier in the SSCS, and warmer and fresher in the JS during the boreal winter, and vice versa during the boreal summer. This could possibly be attributed to the differences in oceanographic processes in the SSCS and the JS during both seasons. Hence, two domain boxes were selected to provide a clearer perspective of the seasonal cycle of SST and SSS; marked as A1 and A2 in Figure 1b to represent SST and SSS in the SSCS and JS, respectively. The seasonal cycle patterns of SST and SSS (Figure 7) derived from the simulated model appeared identical to the CMEMS, MODIS, or WOA, indicating that the model could capture seasonal fluctuations in SST and SSS in both the SSCS and the JS.

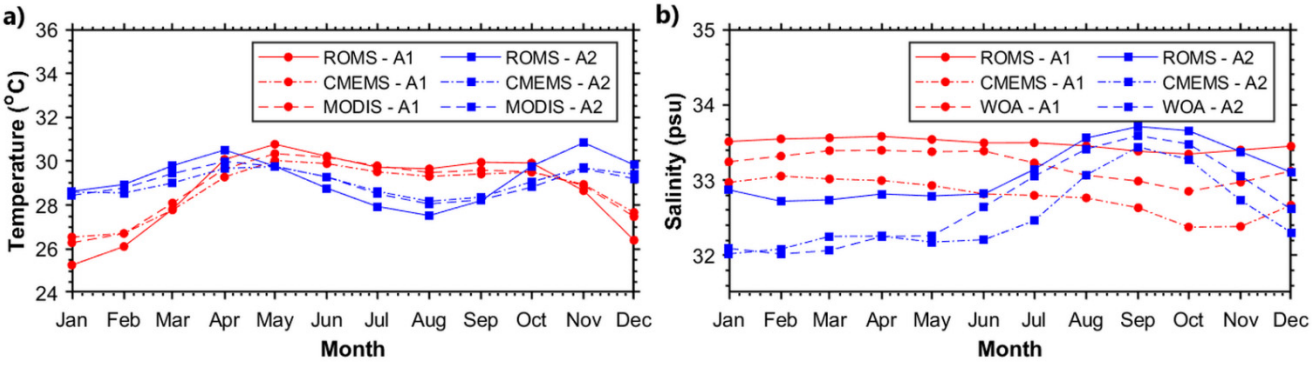

Figure 7. Seasonal cycle of (**a**) SST (unit: °C) and (**b**) SSS (unit: psu) climatology derived from ROMS (solid lines), CMEMS (dash-dot lines), and MODIS/WOA (dashed lines) for Region A1 (red circles) and A2 (blue squares).

It was apparent that the SST in the SSCS was in unimodal distribution, with a maximum value occurring in May. Nonetheless, the SST in the JS was in bimodal distribution, with two maxima in April and November. The SSS in the SSCS was largely consistent throughout the year, but the SSS in the JS was in unimodal distribution with a maximum value occurring in September. The seasonal cycle of SST and SSS in the SSCS and JS may

be associated with the advecting current from its adjacent waters, i.e., northern SCS and Flores Sea [17].

3.5. Water Advection

During the boreal winter, the cooler water that dominated the SSCS led to the formation of a noticeable thermal front along the PMEC and northwest of Borneo (Figure 5a–c). Chu and Wang [82] revealed the existence of a thermal front over the SCS between the Vietnamese Bight and Luzon Island because of a convergence flow in the SCS. This thermal front is advected southward by an intense southward flowing western boundary current located in the continental slope off the eastern Vietnamese coast, creating a tongue of cooler water that results in the formation of this thermal front [56,57,83]. Meanwhile, although the SSCS was dominated by saltier waters, the coastal area was dominated by fresher waters (Figure 6a–c). The seepage of cooler and saltier waters in the SSCS advected southward by the surface current, across the Karimata Strait, and then merged with warmer and fresher waters in the JS. In this particular season, the prevailing monsoon in the SSCS and JS brought considerable precipitation in Southeast Asia [20,70], diluting seawater and resulting in a lower SSS. Although high precipitation hit the study domain, its impacts in the JS were greater, as indicated by lower SSS. This is because the JS is subjected to significant riverine outflow from the neighboring continent, i.e., Sumatra, Java, and south Borneo, as compared with the SSCS. In the JS, the eastward flowing current further advected warmer and fresher waters into the southern Makassar Strait. This advection of fresher waters generated a northward pressure gradient in the Makassar Strait, restricting saltier waters from the Pacific to penetrate southward into the Indian Ocean, which led to the formation of a strong SSS gradient in the southern part of the Makassar Strait [18,20].

During the boreal summer, the eastern part of the JS, i.e., the Flores Sea, was dominated by cooler (Figure 5d–f) and saltier waters (Figure 6d–f), particularly owing to the invasion of wind inducing upwelling water from the southern Makassar Strait (southern tip of the Sulawesi Island) and Banda Sea [18,84–87]. The westward surface current advected cooler and saltier waters from the Flores Sea into the JS, erasing the obstructing northward pressure gradient in the Makassar Strait [18,20]. This allows slightly warmer and saltier waters to flow southward and eventually merged with the cooler and saltier waters from the Flores Sea. In the JS, the fresher waters could still be observed, indicating that the effect of riverine outflow is persistent and appears to dilute saltier water from the Flores Sea, leading to a lower SSS. In the JS, a seepage of cooler and fresher waters was advected northward across the Karimata Strait and entered the SSCS. Fascinatingly, this seepage of cooler and fresher waters was shown to advect onto the PMEC in the path of the strong northward flowing western boundary current, forming a band of cooler and fresher waters between the Karimata Strait and the PMEC. The advected cooler water was basically coalesced with the curl-induced cooler and saltier upwelling waters along the PMEC. After leaving the PMEC, this path of cooler and fresher waters continued to advect towards the Vietnamese coast in the path of the strong northward flowing western boundary current. The advection of cooler waters from the JS towards the SSCS was actually opposed to the previous findings (e.g., Akhir [9]; Cai et al. [88]; Daryabor et al. [12,58,73]; Yanagi et al. [89]), which claimed that a northward flowing current advected warmer tropical waters from the JS, and increased solar radiation led to higher SST in the SSCS during the boreal summer. However, it was apparent that the higher SST in the SSCS probably relied solely on the increase in solar radiation, as the advected waters from the JS were actually cooler.

The advection of cooler water from the JS towards the PMEC during boreal summer supported the previous findings by Kok et al. [56,57,60], but, to the best of the author's knowledge, the advection of fresher water from the JS towards the PMEC has never been documented. This information is critical for the PMEC that are influenced by upwelling because the presence of fresher water along the coast can enhance upwelling via baroclinic pressure gradient force [90]. Nonetheless, it should be emphasized that the advection path of this fresher water was not evident in WOA, most likely owing to a lack of observational

data used to compute gridded salinity in the region, and this situation has been shown by WOA to make it difficult to compute quality control on datasets [91] and should be used with caution [92]. Despite this, the WOA was used to provide a broad picture of the SSS distribution. Because of this constraint, shorter temporal coverage of satellite-derived SSS from Soil Moisture Active Passive (SMAP) with a horizontal resolution of 0.25°, https://smap.jpl.nasa.gov/, accessed on 8 September 2021 [93,94], was employed to offer further information of SSS distribution during the boreal summer (Supplementary Figure S2). The satellite-derived SSS exhibited comparable patterns to ROMS (Figure 6d) and CMEMS (Figure 6e), particular the fresher water path advected from the JS that merged with the saltier upwelling water along the PMEC, supporting the stated feature.

3.6. Seasonal Cycles

The seasonal cycles of SST and SSS (Figure 7) were predominately controlled by the advecting current from the adjacent seas. It should be noted that the selected box in the SSCS (A1) did not cover the PMEC. Hence, the seasonal cycle particularly during the boreal summer where the advection of cooler and fresher waters from the JS towards the PMEC was not reflected here. In the SSCS, the advection of cooler waters from the northern SCS began in November and started to withdraw in February before vanishing in April, leading to lower SST. As the cooler water advection vanished in May, the SST started to rise and was slightly maintained until October. The SSS in the SSCS remained nearly consistent throughout the year, indicating that water advection from its northern part did not significantly alter the SSS. This adds to our understanding of the seasonal cycle of SSS in the SSCS, where the study of salinity is limited owing to a paucity of high-quality observational data [95].

In the JS, the seasonal cycle of SST was predominately affected by cooler water advection from the SSCS and the Flores Sea during the boreal winter and boreal summer, respectively. The advection of cooler water from the SSCS began in December and terminated in March, leading to lower SST. As the advection from the SSCS ceased in April, the SST rose. Immediately after the advection from the SSCS, cooler water from the Flores Sea began to advect into the JS from May, leading to another cooler SST trend that persisted until October. In November, the vanishing of cooler water advection from the Flores Sea resulted in another higher SST. The study of seasonal cycle of SST provides a better understanding of seasonal changes in water characteristics in the JS, with a major focus on salinity, which plays a critical role in the ITF. Unlike SST, the seasonal cycle of SSS in the JS was predominately regulated by saltier water advected from the Flores Sea during the boreal summer, resulting in higher SSS between June and October. It should be noted that the SSS was practically identical in the other months, indicating that the effect of riverine outflow on the SSS in the JS remained consistent throughout the year, unless affected by saltier water advection from the Flores Sea.

3.7. Volume, Freshwater, Heat, and Salt Transports

This section discusses annual and seasonal water transport across the Karimata Strait, i.e., KSTs in terms of volume, freshwater, heat, and salt transport. The estimation of these transports facilitates the understanding of water exchange and interconnection between the SSCS and the JS, which is crucial in affecting the mechanism and development of thermohaline circulation in the region.

3.7.1. Annual Water Transports

Table 1 shows the annual volume, freshwater, heat, and salt transports through the Karimata Strait based on ROMS and various modelling studies. In addition, the configurations and specifications of these models are presented in Table 1. On an annual timescale, all the estimated various transports were directed from the SSCS into the JS. The annual volume, freshwater, heat, and salt transport estimated by ROMS were 0.96 Sv (1 Sv = 10^6 m^3 s^{-1}), 0.04 Sv, 0.10 PW (1 PW = 10^{15} j s^{-1}), and 0.03 × 10^9 kg s^{-1}, respectively,

which was typically higher than the CMEMS estimate of 0.64 Sv, 0.04 Sv, 0.07 PW, and 0.02 $\times$ 10^9 kg s^{-1}, respectively. The computation of Monte Carlo permutation test based on interannual timescales of various transports revealed that the difference between CMEMS and ROMS was significant at a confidence level of 0.05. The existence of this significant difference was attributable to the fact that ROMS had a higher value of various transports' estimation at the interannual timescale, which also explained why ROMS had a higher estimation of annual various transports than CMEMS (not shown).

Table 1. Previous and current estimation of annual volume (F_V; unit: 10^6 m s^{-1}), freshwater (F_W; unit: 10^6 m s^{-1}), heat (F_H; unit: 10^{15} j s^{-1}), and salt (F_S; unit: 10^9 kg s^{-1}) transports.

Author	Model	Domain	Horizontal Resolution (°)	Vertical Resolution	Annual Transport			
					F_V	F_W	F_H	F_S
Fang et al. [25]	MOM Version 2	Outer: Global Ocean Inner: SCS, East China Sea, Japan/East Sea	Outer: 3 Inner: 1/6	15 levels	3.15	-	0.35	0.11
Cai et al. [24]	LICOM	75° S–65° N	1/2	12 levels	1.86	-	0.17	0.07
Fang et al. [26]	MOM Version 2	Outer: 87° N–Southern Antarctic Coast Inner: 20° S–60° N, 98–156° E	Outer: ±2 Inner: 1/6	18 levels	1.16	0.05	0.11	0.04
-	CMEMS	Global Ocean	1/12	50 z-levels	0.64	0.04	0.07	0.02
Present Study	ROMS	23.65° S–25.97° N, 98.82–142.22° E	1/20 × 1/25	30 levels	0.96	0.04	0.10	0.03

In comparison with other modelling studies, the estimated various transports indicated a great deal of variation. The estimated annual volume, freshwater, heat, and salt transports by all the listed models range from 0.64 to 3.15 Sv, 0.04 to 0.05 Sv, 0.07 to 0.35 PW, and 0.02 to 0.11 $\times$ 10^9 kg s^{-1}, respectively. Owing to the different configurations and specifications of the ocean models, the significant discrepancy in the estimated various water transports was possibly expected.

The present ocean model and CMEMS provide lower estimations of volume, freshwater, heat, and salt transports. This could be because of the finer horizontal and vertical resolutions of ROMS and CMEMS, as well as the distinct turbulent diffusion periods attributed to vertical turbulent and the vertical advection of convection of the layer, which could result in lower estimates of various transports.

3.7.2. Seasonal Water Transports

Volume transport estimation showed seasonal fluctuations, with a higher value during the boreal winter and a lower value during the boreal summer (Figure 8a). The seasonal volume transport pattern of the model was generally consistent with that of CMEMS; however, ROMS had a higher value, as in the case of annual volume transport. The volume transport estimated by ROMS and CMEMS in January was 3.31 Sv and 1.66 Sv, respectively, which corresponded to the predominantly southward current across the Karimata Strait during the boreal winter (Figure 4a,b). The volume transport gradually decreased from January to April before turning negative (inflow from the JS into the SSCS) between May and August, when the current was mostly northward (Figure 4c,d). However, in May, volume transport estimated by ROMS (−1.23 Sv) was the highest among the months with negative volume transport, contrasting with CMEMS, which recorded approximately comparable volume transport. The anticyclonic eddy captured by ROMS during the boreal summer in the southern part of the SSCS (Supplementary Figure S1) was also visible in May, but it was slightly stronger and larger (not shown). The western northward flowing part of this anticyclonic eddy penetrated the Karimata Strait, contributing to the stronger northward volume transport in May. As stated earlier, this anticyclonic eddy

was not captured by CMEMS, explaining why the northward volume transport estimated by ROMS peaked in May, but not in CMEMS. In June, as the anticyclonic weakened, the volume transport estimated by ROMS decreased, and the trend of volume transport between ROMS and CMEMS was similar. Except for ROMS estimation in May, volume transport peaked around June and July (−1.17 Sv by ROMS and −0.45 Sv CMEMS) before declining in August. In September, the volume transport was nearly zero and turned back to positive over the remaining months with an increasing trend when the current was mostly southward. Therefore, volume transport across the Karimata Strait appeared to be predominantly influenced by the monsoon cycle. Aside from CMEMS, volume transport was compared to estimates made by Fang et al. [25], who utilized a global ocean model with a coarser horizontal and vertical resolution of 1/6° and 15 levels, respectively. In general, Fang et al.'s [25] model appeared to overestimate the volume transport when compared with ROMS and CMEMS, especially during the outflow from the SSCS into the JS. This implied that a coarser horizontal and vertical resolution of ocean model, such as that used by Fang et al. [25], would likely to provide higher volume transport, especially in shallow regions and when the strait is connected to the different regions, as suggested by Fang et al. [27], as in the case of the Karimata Strait.

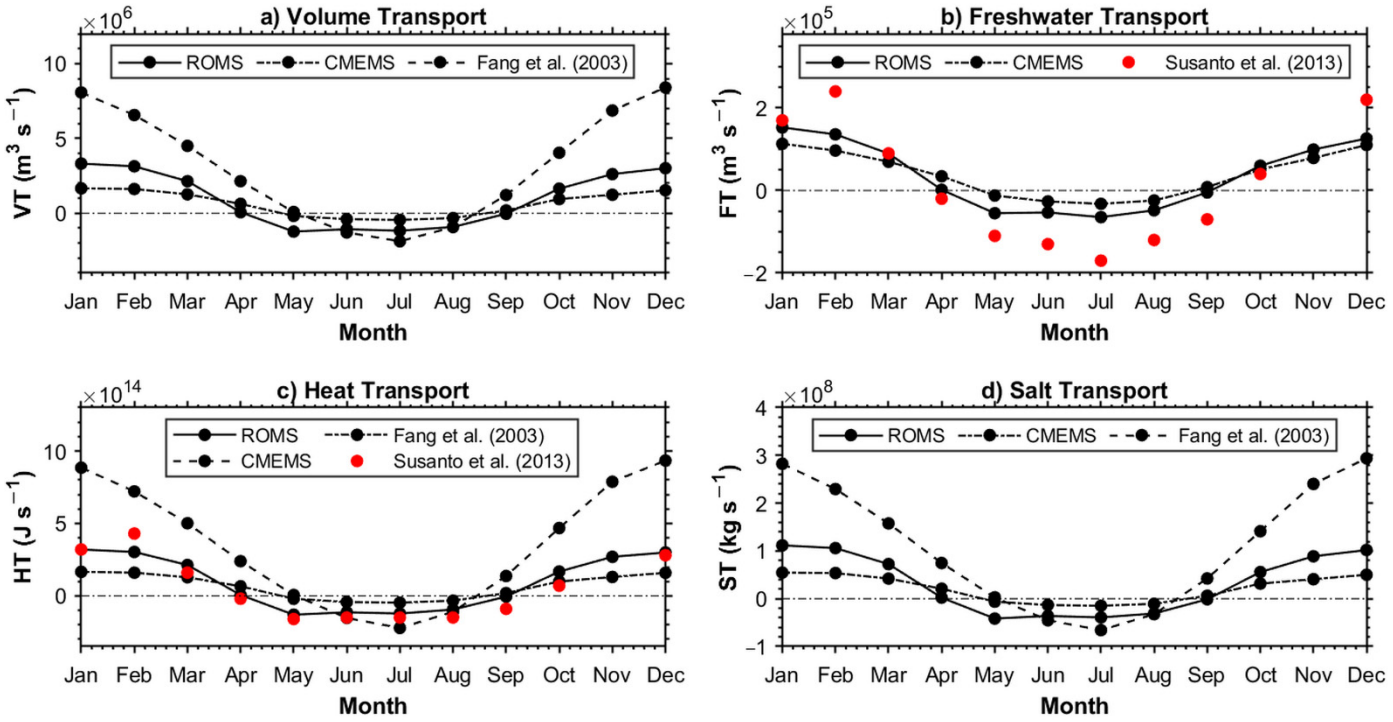

Figure 8. Seasonal variability of (**a**) volume (unit: $m^3\ s^{-1}$), (**b**) freshwater (unit: $m^3\ s^{-1}$), (**c**) heat (unit: $J\ s^{-1}$), and (**d**) salt (unit: $kg\ s^{-1}$) transports derived from ROMS (solid line), CMEMS (dashed-dot line), Fang et al. [25] (dashed-line), and Susanto et al. [22] (red circles). Positive values denote the outflow from the SSCS though the Karimata Strait into the JS, while negative values denote the inflow from the JS through the Karimata Strait into the SSCS.

The freshwater transport pattern derived from ROMS and CMEMS was roughly proportional to volume transport (Figure 8b). According to ROMS and CMEMS, freshwater water transport peaked in January during the outflow months from the SSCS into the JS. During the inflow months from the JS into the SSCS, the freshwater transport estimated by ROMS peaked in May, but CMEMS peaks in July, highlighting the role of the simulated anticyclonic eddy in causing this situation. With the deployment of trawl-resistant bottom mounts equipped with ADCPs and salinity data obtained from field observations and the WOA, Susanto et al. [22] estimated freshwater transport between December 2007 and October 2008. According to the presented chart, the freshwater transport estimated by

Susanto et al. [22] was positive from January to March and October to December, and negative from April to September. The direction of ROMS estimation was the same as in Susanto et al. [22]; however, the estimations of Susanto et al. [22] were primarily of a qualitative nature, and actual freshwater transport is still subjected to further investigation. Nevertheless, the freshwater transport estimated by Susanto et al. [22] appeared to be much greater than ROMS and CMEMS, in contrast to heat transport estimation (Figure 8c), where ROMS, CMEMS, and Susanto et al. [22] did not differ significantly. One possible explanation is that Susanto et al. [22] used limited salinity data to estimate freshwater transport, which relied solely on single point measurement, and sparse WOA data, which made it impossible to perform an appropriate estimate, particularly between May and September, when freshwater transport was significantly lower.

The heat transport estimated by ROMS and CMEMS across the Karimata Strait was comparable to the volume transport (Figure 8c). Nevertheless, the heat transport estimation of ROMS displayed a more consistent trend with Susanto et al.'s [22] field observations, particularly in May, when the transport was largely influenced by the anticyclonic eddy, resulting in the maximum heat transport. In general, similar to the volume transport, the heat transport estimated by Fang et al.'s [25] model was higher than the estimation of ROMS, CMEMS, and Susanto et al. [22], especially during the outflow months from the SSCS into the JS.

Likewise, the estimated salt transport across the Karimata Strait reflected the volume transport fluctuation (Figure 8d). Among the months with positive salt transport, the highest salt transport into the JS was 1.1×10^8 kg s^{-1} in January, which corresponded to the CMEMS estimate (0.55×10^8 kg s^{-1}). Under the influence of anticyclonic eddy, the salt transport estimated by ROMS was at its peak in May (-0.42×10^8 kg s^{-1}) among the months with negative salt transport. However, as the anticyclonic eddy drifted away from the Karimata Strait, it recorded another peak in July (-0.39×10^8 kg s^{-1}), corresponding to the CMEMS of -0.15×10^9 kg s^{-1}. Again, similar to volume, freshwater, and heat transports, Fang et al. [21] appeared to have higher estimates of salt transport, especially during the outflow months from the SSCS into the JS.

Our study provided new information in which all the estimated various KSTs, i.e., volume, freshwater, heat, and salt transports, peaked in May during the inflow from the JS into the SSCS because of the presence of stronger anticyclonic eddy in the southern part of the SSCS in May, which differs from the aforementioned dataset and previous studies (e.g., Daryabor et al. [12,13]; Wyrtki [96]) that estimated that various KSTs peaked between June and August.

4. Summary and Conclusions

In this study, a ROMS model application, forced with an appropriate atmospheric and oceanic forcing, was used to simulate the water circulations and its associated volume, freshwater, heat, and salt transports between the SSCS and the JS to investigate the interconnection between these two water bodies across the Karimata Strait. The simulated ocean dynamics between the SSCS and the JS basically established a good agreement with the various datasets.

The seasonal surface current in the study domain was influenced by the monsoonal wind stress with the presence of reversing surface current flow in the SSCS and JS. During the boreal winter, a strong western boundary current was observed to flow southward from the PMEC into the JS via the Karimata Strait, whereas during the boreal summer, the western boundary current was reversed, flowing from the JS to the PMEC. Furthermore, the cyclonic structure dominated the SSCS during the boreal winter, while the dual anticyclonic structures dominated during the boreal summer.

The seasonal variability of SST and SSS patterns between the SSCS and the JS was influenced by the water exchanges between these two bodies of water. During the boreal winter, cooler and saltier waters were advected southward from the SSCS through the Karimata Strait into the JS. However, during the boreal summer, cooler and fresher waters

from the JS were advected into the SSCS, forming a clear advection path that extended between the JS and the PMEC according to the path of the northward flowing western boundary current.

The seasonal various KSTs, i.e., the volume of freshwater, heat, and salt transports across the Karimata Strait, followed the water circulation patterns between the SSCS and the JS. The various water transports directed southward from the SSCS into the JS via the Karimata Strait, which was consistent with the mainly southward flow in the Karimata Strait during the boreal winter. Meanwhile, the various KSTs were reversed during the boreal winter, driven from the JS into the SSCS when the Karimata Strait circulations were predominantly northward. The finer horizontal and vertical resolutions of the present model were believed to have a better estimation of various water transports than coarser resolutions of global ocean model by Fang et al. [25]. This could be attributable to the ability of the finer resolutions ocean model to deal with the complexity of the shallow Karimata Strait, which experiences rapid fluctuations caused by interaction with topography and bathymetry. The estimated annual means of the various KSTs were all directed southward into the JS from the SSCS, reporting 0.96 Sv, 0.04 Sv, 0.10 PW, and 0.03×10^9 kg s^{-1} for the volume of freshwater, heat, and salt transports, respectively, as estimated by ROMS.

It is worth noting that the simulated results derived from this study are primary validated against the CMEMS instead of observational data. The justification for this is that there is a lack of observational data available in this region; thus, the CMEMS was used to act as our pseudo-observational data for validating ROMS because CMEMS assimilates a number of observation data sources, and previous findings indicated that the data assimilation technique can produce a reliable dataset [97–99]. Indeed, numerous studies employed the assimilated ocean model to evaluate their produced ocean model [12,13,58]. Although most of the datasets can be obtained directly from the CMEMS, the rationale for developing a new ocean model, as done in this study, may be questioned. It should be noted that the horizontal resolution of CMEMS is $1/12^\circ$, which is slightly coarser than the present ocean model, which has a finer horizontal resolution of $1/20^\circ$. The use of a higher resolution ocean model is required because it enhances model accuracy and allows for the simulation of small-scale processes, reducing reliance on uncertain parameterizations [100]. This is demonstrated by the successful simulation of mesoscale features of dual anticyclonic eddies off the PMEC during the boreal summer using the present higher resolution ocean model, which was absent in the CMEMS with a slightly coarser horizontal resolution.

We would like to point out that there is a lack of in situ data in the region to validate some of the major regional features simulated by ROMS, particularly the surface current. However, the development of this ROMS model is truly timely, as it fills a gap in the region where observational data are scarce, and this study can inspire regional collaboration to conduct field observations for a better understanding of oceanographic conditions within the SSCS and the JS.

Supplementary Materials: The following are available online at https://www.mdpi.com/article/10.3390/jmse9101040/s1, Figure S1: Climatology of surface current (unit: m s^{-1}) derived from ROMS in June, July, and August. Figure S2: Seasonal SSS (unit: psu) climatology during the boreal summer derived from SMAP.

Author Contributions: Conceptualization, P.H.K., S.W., M.F.A., and C.P.; methodology, P.H.K., S.W., M.F.A., and C.P.; validation, P.H.K., S.W., and F.S.M.A.; formal analysis, P.H.K., S.W., and N.H.R.; investigation, P.H.K., S.W., and N.H.R.; resources, S.W. and C.P.; data curation, P.H.K. and S.W.; writing—original draft preparation, P.H.K. and N.H.R.; writing—review and editing, M.F.A., C.P., and F.S.M.A.; visualization, P.H.K.; supervision, M.F.A., S.W., and C.P.; project administration, M.F.A.; funding acquisition, M.F.A. All authors have read and agreed to the published version of the manuscript.

Funding: This research was funded by the Higher Institution Centre of Excellence (HICoE) grant awarded to the Institute of Oceanography and Environment (INOS), Universiti Malaysia Terengganu (UMT) by Ministry of Higher Education (MoHE), Malaysia, grant number TJ 66928; International

Collaboration Fund (ICF) provided by the Ministry of Science, Technology, and Innovation (MOSTI), grant number UMT0070814; and Long-Term Research Grant Scheme (LRGS) provided by MoHE, Malaysia, grant number LRGS/1/2020/UMT/01/1.

Institutional Review Board Statement: Not applicable.

Informed Consent Statement: Not applicable.

Data Availability Statement: Publicly available datasets were analyzed in this study. The data can be obtained by following the link provided in the manuscript.

Acknowledgments: This work was supported by resources provided by the Pawsey Supercomputing Centre with funding from the Australian Government and the Government of Western Australia acquired by Charitha Pattiaratchi and Sarath Wijeratne.

Conflicts of Interest: The authors declare no conflict of interest. The funders had no role in the design of the study; in the collection, analyses, or interpretation of data; in the writing of the manuscript; or in the decision to publish the results.

References

1. Fang, G.; Chen, H.; Wei, Z.; Wang, Y.; Wang, X.; Li, C. Trends and interannual variability of the South China Sea surface winds, surface height, and surface temperature in the recent decade. *J. Geophys. Res. Space Phys.* **2006**, *111*, 1–16. [CrossRef]
2. Wyrtki, K. Physical Oceanography of the Southeast Asian Waters. In *NAGA Report*; University of California: La Jolla, LA, USA, 1961; Volume 2, p. 195.
3. Taira, K.; Saadon, M.N.B.; Kitagawa, S.; Yanagi, T. Observation of temperature and velocity in the coastal water off Kuala Terengganu, Malaysia. *J. Oceanogr.* **1996**, *52*, 251–257. [CrossRef]
4. Morgan, J.R.; Valencia, M.J. The Natural Environmental Setting. In *Atlas for Marine Policy in Southeast Asian Seas*; Morgan, J.R., Valencia, M.J., Eds.; University of California: La Jolla, LA, USA, 1983; pp. 4–17.
5. Sadhomoto, B. Review of environmental features of the Java Sea. *Indones. Fish Res. J.* **2006**, *12*, 129–157. [CrossRef]
6. Hendiarti, N.; Siegel, H.; Ohde, T. Investigation of different coastal processes in Indonesian waters using SeaWiFS data. *Deep. Sea Res. Part II Top. Stud. Oceanogr.* **2004**, *51*, 85–97. [CrossRef]
7. Dale, W.L. Winds and drift currents in the South China Sea. *Malays. J. Trop Geogr.* **1956**, *8*, 1–31.
8. Liu, Q.; Feng, M.; Wang, D. ENSO-induced interannual variability in the southeastern South China Sea. *J. Oceanogr.* **2011**, *67*, 127–133. [CrossRef]
9. Akhir, M.F.M. Surface circulation and temperature distribution of southern South China Sea from Global Ocean Model (OCCAM). *Sains Malays.* **2012**, *41*, 701–714.
10. Tangang, F.; Xia, C.; Qiao, F.; Juneng, L.; Shan, F. Seasonal circulations in the Malay Peninsula Eastern continental shelf from a wave-tide-circulation coupled model. *Ocean Dyn.* **2011**, *61*, 1317–1328. [CrossRef]
11. Fang, G.; Fang, W.; Fang, Y.; Wang, K. A survey of studies on the South China sea upper ocean circulation. *Acta Oceanogr. Taiwanica.* **1998**, *37*, 1–16.
12. Daryabor, F.; Samah, A.A.; Ooi, S.H.; Chenoli, S.N. An estimate of the Sunda Shelf and the Strait of Malacca transports: A nu-merical study. *Ocean Sci. Discuss.* **2015**, *12*, 275–313. [CrossRef]
13. Daryabor, F.; Ooi, S.H.; Abu Samah, A.; Akbari, A. Dynamics of the Water Circulations in the Southern South China Sea and Its Seasonal Transports. *PLoS ONE* **2016**, *11*, e0158415. [CrossRef]
14. Atmadipoera, A.S.; Kusmanto, E.; Purwandana, A.; Nurjaya, I.W. Observation of coastal front and circulation in the north-eastern Java Sea, Indonesia. *J. Ilmu. dan Teknol. Kelaut. Trop.* **2015**, *7*, 91–108.
15. Qu, T. Role of ocean dynamics in determining the mean seasonal cycle of the South China Sea surface temperature. *J. Geophys. Res. Space Phys.* **2001**, *106*, 6943–6955. [CrossRef]
16. Durand, J.R.; Petit, D. The Java Sea Environment. In *Biology, Dynamics, Exploitation of the Small Pelagic Fishes in the Java Sea*; Potier, M., Nurhakim, S., Eds.; Agency for Agricultural Research and Development: Jakarta, Indonesia, 1995; pp. 15–38.
17. Qu, T.; Du, Y.; Sasaki, H. South China Sea throughflow: A heat and freshwater conveyor. *Geophys. Res. Lett.* **2006**, *33*, 1–4. [CrossRef]
18. Gordon, A. Oceanography of the Indonesian Seas and Their Throughflow. *Oceanography* **2005**, *18*, 14–27. [CrossRef]
19. Sofian, I. Simulation of the Java Sea using an oceanic general circulation model. *J. Ilmu. Geomatika.* **2007**, *13*, 1–14.
20. Gordon, A.L.; Susanto, R.D.; Vranes, K. Cool Indonesian throughflow as a consequence of restricted surface layer flow. *Nature* **2003**, *425*, 824–828. [CrossRef] [PubMed]
21. Fang, G.; Susanto, R.D.; Wirasantosa, S.; Qiao, F.; Supangat, A.; Fan, B.; Wei, Z.; Sulistiyo, B.; Li, S. Volume, heat, and freshwater transports from the South China Sea to Indonesian seas in the boreal winter of 2007–2008. *J. Geophys. Res. Space Phys.* **2010**, *115*. [CrossRef]
22. Susanto, R.D.; Wei, Z.; Adi, R.T.; Fan, B.; Li, S.; Fang, G. Observations of the Karimata Strait througflow from December 2007 to November 2008. *Acta Oceanol. Sin.* **2013**, *32*, 1–6. [CrossRef]

23. He, Z.; Feng, M.; Wang, D.; Slawinski, D. Contribution of the Karimata Strait transport to the Indonesian Throughflow as seen from a data assimilation model. *Cont. Shelf Res.* **2015**, *92*, 16–22. [CrossRef]
24. Cai, S.; Liu, H.; Long, X. Application of LICOM to the numerical study of water exchange between the South China Sea and its adjacent oceans. *Acta Oceanol. Sin.* **2005**, *24*, 10–19.
25. Fang, G.; Wei, Z.; Choi, B.-H.; Wang, K.; Fang, Y.; Li, W. Interbasin freshwater, heat and salt transport through the boundaries of the East and South China Sea from a variable-grid ocean circulation model. *Sci. China (Ser. D)* **2003**, *46*, 149–161. [CrossRef]
26. Fang, G.; Wang, Y.; Wei, Z.; Fang, Y.; Qiao, F.; Hu, X. Interocean circulation and heat and freshwater budgets of the South China Sea based on a numerical model. *Dyn. Atmos. Oceans* **2009**, *47*, 55–72. [CrossRef]
27. Guohong, F.; Susanto, D.; Soesilo, I.; Zheng, Q.; Fangli, Q.; Zexun, W. A note on the South China Sea shallow interocean circulation. *Adv. Atmos. Sci.* **2005**, *22*, 946–954. [CrossRef]
28. Shchepetkin, A.F.; McWilliams, J.C. The regional oceanic modeling system (ROMS): A split-explicit, free-surface, topography-following-coordinate oceanic model. *Ocean Model.* **2005**, *9*, 347–404. [CrossRef]
29. Haidvogel, D.B.; Arango, H.; Budgell, W.P.; Cornuelle, B.D.; Curchitser, E.; Di Lorenzo, E.; Fennel, K.; Geyer, W.R.; Hermann, A.J.; Lanerolle, L.; et al. Ocean forecasting in terrain-following coordinates: Formulation and skill assessment of the Regional Ocean Modeling System. *J. Comput. Phys.* **2008**, *227*, 3595–3624. [CrossRef]
30. GEBCO Bathymetric Compilation Group. *The GEBCO_2019 Grid—A Continuous Terrain Model of the Global Oceans and Land*; British Oceanographic Data Centre, National Oceanography Centre: Southampton, UK, 2019.
31. Sikirić, M.D.; Janeković, I.; Kuzmić, M. A new approach to bathymetry smoothing in sigma-coordinate ocean models. *Ocean Model.* **2009**, *29*, 128–136. [CrossRef]
32. Copernicus Climate Change Service (C3S). Fifth Generation of ECMWF Atmospheric Reanalyses of the Global Climate. In *ERA5 Fifth Gener ECMWF Atmos Reanalyses Glob Clim*; Copernicus Climate Change Service (C3S): Reading, UK, 2017.
33. Cummings, J.A. Operational multivariate ocean data assimilation. *Q. J. R. Meteorol. Soc.* **2005**, *131*, 3583–3604. [CrossRef]
34. Cummings, J.A.; Smedstad, O.M. *Variational Data Assimilation for the Global Ocean*; Springer: Berlin/Heidelberg, Germany, 2013; pp. 303–343. [CrossRef]
35. Fox, D.N.; Teague, W.J.; Barron, C.N.; Carnes, M.R.; Lee, C.M. The Modular Ocean Data Assimilation System (MODAS). *J. Atmos. Ocean Technol.* **2002**, *19*, 240–252. [CrossRef]
36. Wijeratne, S.; Pattiaratchi, C.; Proctor, R. Estimates of Surface and Subsurface Boundary Current Transport Around Australia. *J. Geophys. Res. Oceans* **2018**, *123*, 3444–3466. [CrossRef]
37. Marchesiello, P.; McWilliams, J.C.; Shchepetkin, A.F. Open boundary conditions for long-term integration of regional oceanic models. *Ocean Model.* **2001**, *3*, 1–20. [CrossRef]
38. Egbert, G.D.; Erofeeva, S.Y. Efficient inverse modeling of barotropic ocean tides. *J. Atmos. Ocean Technol.* **2002**, *19*, 183–204. [CrossRef]
39. Flather, R.A. A tidal model of the north-west European continental shelf. *Mem. Soc. R. Sci. Liege.* **1976**, *6*, 141–164.
40. Chapman, D.C. Numerical Treatment of Cross-Shelf Open Boundaries in a Barotropic Coastal Ocean Model. *J. Phys. Oceanogr.* **1985**, *15*, 1060–1075. [CrossRef]
41. Barnier, B.; Siefridt, L.; Marchesiello, P. Thermal forcing for a global ocean circulation model using a three-year climatology of ECMWF analyses. *J. Mar. Syst.* **1995**, *6*, 363–380. [CrossRef]
42. Maltrud, M.E.; Smith, R.D.; Semtner, A.J.; Malone, R.C. Global eddy-resolving ocean simulations driven by 1985–1995 atmospheric winds. *J. Geophys. Res. Ocean* **1998**, *103*, 30825–30853. [CrossRef]
43. Barth, A.; Alvera-Azcárate, A.; Beckers, J.-M.; Rixen, M. Coupling a two-way nested primitive equation model and a statistical SST predictor of the Ligurian Sea via data assimilation. *Ocean Model.* **2006**, *13*, 255–270. [CrossRef]
44. Gordon, A.L.; Huber, B.A.; Metzger, E.J.; Susanto, R.D.; Hurlburt, H.E.; Adi, T.R. South China Sea throughflow impact on the Indonesian throughflow. *Geophys. Res. Lett.* **2012**, *39*, 1–7. [CrossRef]
45. Seo, H.; Xie, S.-P.; Murtugudde, R.; Jochum, M.; Miller, A.J. Seasonal Effects of Indian Ocean Freshwater Forcing in a Regional Coupled Model. *J. Clim.* **2009**, *22*, 6577–6596. [CrossRef]
46. Guilyardi, E.; Swingedouw, D.; Mignot, J.; Labetoulle, S.; Servonnat, J.; Séférian, R. Reconstructing the subsurface ocean decadal variability using surface nudging in a perfect model framework. *Clim. Dynam.* **2015**, *44*, 315–338. [CrossRef]
47. Holgate, S.J.; Matthews, A.; Philip, L.; Woodworth, L.J.R.; Tamisiea, M.E.; Bradshaw, E.; Foden, P.R.; Gordon, K.M.; Jevrejeva, S.; Pugh, J. New data systems and products at the Permanent Service for Mean Sea Level. *J. Coast Res.* **2013**, *29*, 493–504. [CrossRef]
48. Fernandez, E.; Lellouche, J.M. *Product User Manual for the Global Ocean Physical Reanalysis Product GLOBAL_REANALYSIS_PHY_001_030*; Corpernicus Marine Service: Toulouse, France, 2021; Volume 2.1, 21p.
49. Drévillon, M.; Lellouche, J.-M.; Régnier, C.; Garric, G.; Bricaud, C.; Hernandez, O.; Bourdallé-Badie, R. *Quality Information Document for GLOBAL_REANALYSIS_PHY_001_030*; Corpernicus Marine Service: Toulouse, France, 2021; Volume 1.4, 52p.
50. Lorente, P.; García-Sotillo, M.; Amo-Baladrón, A.; Aznar, R.; Levier, B.; Sánchez-Garrido, J.C.; Sammartino, S.; De Pascual, A.; Reffray, G.; Toledano, C.; et al. Skill assessment of global, regional, and coastal circulation forecast models: Evaluating the benefits of dynamical downscaling in IBI (Iberia–Biscay–Ireland) surface waters. *Ocean Sci.* **2019**, *15*, 967–996. [CrossRef]
51. Feldman, G.C.; McClian, C.R. *Terra & Aqua—MODIS Reprocessing*; Kuring, N., Bailey, S.W., Eds.; Ocean Color Web: Greenbelt, ML, USA, 2014.

52. Boyer, T.P.; Garcia, H.E.; Locarnini, R.A.; Zweng, M.M.; Mishonov, A.V.; Reagan, J.R.; Weathers, K.A.; Baranova, O.K.; Paver, C.R.; Seidov, D.; et al. World Ocean Atlas. 2018 [Internet]. NOAA National Centers for Environmental Information. 2018. Available online: https://accession.nodc.noaa.gov/NCEI-WOA18 (accessed on 18 August 2021).
53. Levitus, S.; Boyer, T. *World Ocean Atlas*; National Oceanic and Atmospheric Administration: Washington, DC, USA, 1994; 117p.
54. Ffield, A.; Gordon, A.L.; Susanto, R.D.; Garzoli, S.L.; Vranes, K. Temperature variability within Makassar Strait. *Geophys. Res. Lett.* **2000**, *27*, 237–240. [CrossRef]
55. Schiller, A.; Godfrey, J.S.; McIntosh, P.C.; Meyers, G.; Wijffels, S. Seasonal Near-Surface Dynamics and Thermodynamics of the Indian Ocean and Indonesian Throughflow in a Global Ocean General Circulation Model. *J. Phys. Oceanogr.* **1998**, *28*, 2288–2312. [CrossRef]
56. Kok, P.H.; Akhir, M.F.; Tangang, F. Thermal frontal zone along the east coast of Peninsular Malaysia. *Cont. Shelf Res.* **2015**, *110*, 1–15. [CrossRef]
57. Kok, P.H.; Akhir, M.F.M.; Tangang, F.; Husain, M.L. Spatiotemporal trends in the southwest monsoon wind-driven upwelling in the southwestern part of the South China Sea. *PLoS ONE* **2017**, *12*, e0171979. [CrossRef]
58. Daryabor, F.; Tangang, F.; Juneng, L. Simulation of southwest monsoon current circulation and temperature in the east coast of peninsular Malaysia. *Sains Malays.* **2014**, *43*, 389–398.
59. Akhir, M.F.; Daryabor, F.; Husain, M.L.; Tangang, F.; Qiao, F. Evidence of upwelling along Peninsular Malaysia during south-west monsoon. *Open J. Mar. Sci.* **2015**, *5*, 273–279. [CrossRef]
60. Kok, P.H.; Akhir, M.F.; Qiao, F. Distinctive characteristics of upwelling along the Peninsular Malaysia's east coast during 2009/10 and 2015/16 El Niños. *Cont. Shelf Res.* **2019**, *184*, 10–20. [CrossRef]
61. Pickett, M.H.; Paduan, J.D. Ekman transport and pumping in the California Current based on the U.S. Navy's high-resolution atmospheric model (COAMPS). *J. Geophys. Res.* **2003**, *108*, 1–10. [CrossRef]
62. Castelao, R.M.; Barth, J.A. Upwelling around Cabo Frio, Brazil: The importance of wind stress curl. *Geophys. Res. Lett.* **2006**, *33*, 1–4. [CrossRef]
63. Pérez-Santos, I.; Schneider, W.; Sobarzo, M.; Montoya-Sánchez, R.; Valle-Levinson, A.; Garcés-Vargas, J. Surface wind variability and its implications for the Yucatan basin–Caribbean Sea dynamics. *J. Geophys. Res. Space Phys.* **2010**, *115*, 1–15. [CrossRef]
64. Tkalich, P.; Vethamony, P.; Babu, M.T.; Malanotte-Rizzoli, P. Storm surges in the Singapore Strait due to winds in the South China Sea. *Nat. Hazards* **2012**, *66*, 1345–1362. [CrossRef]
65. Minola, L.; Zhang, F.; Azorin-Molina, C.; Pirooz, A.A.S.; Flay, R.G.J.; Hersbach, H.; Chen, D. Near-surface mean and gust wind speeds in ERA5 across Sweden: Towards an improved gust parametrization. *Clim. Dyn.* **2020**, *55*, 887–907. [CrossRef]
66. Jiang, Y.; Han, S.; Shi, C.; Gao, T.; Zhen, H.; Liu, X. Evaluation of HRCLDAS and ERA5 Datasets for Near-Surface Wind over Hainan Island and South China Sea. *Atmosphere* **2021**, *12*, 766. [CrossRef]
67. Liu, Y.; Lin, M.; Jiang, X.; Sun, X.; Song, X. A comparison of multiplatform wind products in the South China Sea during summer and autumn in 2019. *J. Oceanol. Limnol.* **2021**, 1–14. [CrossRef]
68. Wyrtki, K. Die Zirkulation an der Oberfläche der südostasiatischen Gewässer. *Dtsch. Hydrogr. Z.* **1957**, *10*, 1–13. [CrossRef]
69. Mayer, B.; Damm, P.E. The Makassar Strait throughflow and its jet. *J. Geophys. Res. Space Phys.* **2012**, *117*, 1–14. [CrossRef]
70. Tozuka, T.; Qu, T.; Yamagata, T. Dramatic impact of the South China Sea on the Indonesian Throughflow. *Geophys. Res. Lett.* **2007**, *34*, 1–5. [CrossRef]
71. Du, Y.; Qu, T. Three inflow pathways of the Indonesian throughflow as seen from the simple ocean data assimilation. *Dyn. Atmos. Oceans* **2010**, *50*, 233–256. [CrossRef]
72. Chu, P.; Edmons, N.L.; Fan, C. Dynamical Mechanisms for the South China Sea Seasonal Circulation and Thermohaline Variabilities. *J. Phys. Oceanogr.* **1999**, *29*, 2971–2989. [CrossRef]
73. Daryabor, F.; Abu Samah, A.; Ooi, S.H. Dynamical structure of the sea off the east coast of Peninsular Malaysia. *Ocean Dyn.* **2014**, *65*, 93–106. [CrossRef]
74. Susanto, R.D.; Fang, G.; Soesilo, I.; Zheng, Q.; Qiao, F.; Wei, Z.; Sulistyo, B. New Surveys of a Branch of the Indonesian Throughflow. *Eos* **2010**, *91*, 261–263. [CrossRef]
75. Sprintall, J.; Wijffels, S.; Gordon, A.L.; Ffield, A.; Molcard, R.; Susanto, R.D.; Soesilo, I.; Sopaheluwakan, J.; Surachman, Y.; Van Aken, H.M. Instant: A new international array to measure the Indonesian Throughflow. *Eos* **2004**, *85*, 369–376. [CrossRef]
76. Rhines, P.B.; Eddies, M. *Encyclopedia of Ocean Sciences*; Steele, J.H., Ed.; Elsevier: Cambridge, UK, 2001; pp. 1717–1730.
77. Chelton, D.B.; Schlax, M.G.; Samelson, R.M. Global observations of nonlinear mesoscale eddies. *Prog. Oceanogr.* **2011**, *91*, 167–216. [CrossRef]
78. McGillicuddy, D.J.; Robinson, A.R.; Siegel, D.A.; Jannasch, H.W.; Johnson, R.; Dickey, T.D.; McNeil, J.; Michaels, A.F.; Knap, A.H. Influence of mesoscale eddies on new production in the Sargasso Sea. *Nature* **1998**, *394*, 263–266. [CrossRef]
79. Garçon, V.C.; Oschlies, A.; Doney, S.; McGillicuddy, D.; Waniek, J. The role of mesoscale variability on plankton dynamics in the North Atlantic. *Deep. Sea Res. Part II Top. Stud. Oceanogr.* **2001**, *48*, 2199–2226. [CrossRef]
80. Robinson, A.R.; Leslie, W.G.; Theocharis, A.; Lascaratos, A. Mediterranean Sea Circulation. In *Encyclopedia of Ocean Sciences*; Steele, J.H., Ed.; Academic Press: Cambridge, UK, 2001; pp. 1689–1705.
81. Lonin, S.A.; Hernández, J.L.; Palacios, D.M. Atmospheric events disrupting coastal upwelling in the southwestern Caribbean. *J. Geophys. Res. Space Phys.* **2010**, *115*, 1–4. [CrossRef]

82. Chu, P.C.; Wang, G. Seasonal variability of thermohaline front in the central South China Sea. *J. Oceanogr.* **2003**, *59*, 65–78. [CrossRef]
83. Liu, Q.; Jiang, X.; Liu, W.T. A gap in the Indo-Pacific warm pool over the South China Sea in boreal winter: Seasonal development and interannual variability. *J. Geophys. Res.* **2004**, *109*, 1–10. [CrossRef]
84. Utama, F.G.; Atmadipoera, A.; Purba, M.; Sudjono, E.H.; Zuraida, R. Analysis of upwelling event in Southern Makassar Strait. *IOP Conf. Ser. Earth Environ. Sci.* **2017**, *54*, 12085. [CrossRef]
85. Ffield, A.; Gordon, A.L. Vertical Mixing in the Indonesian Thermocline. *J. Phys. Oceanogr.* **1992**, *22*, 184–195. [CrossRef]
86. Nababan, B.; Rosyadi, N.; Manurung, D.; Natih, N.M.; Hakim, R. The Seasonal Variability of Sea Surface Temperature and Chlorophyll-a Concentration in the South of Makassar Strait. *Procedia Environ. Sci.* **2016**, *33*, 583–599. [CrossRef]
87. Susanto, R.D.; Moore, T.; Marra, J. Ocean color variability in the Indonesian Seas during the SeaWiFS era. *Geochem. Geophys. Geosyst.* **2006**, *7*, 1–16. [CrossRef]
88. Cai, S.; Su, J.; Long, X.; Wang, S.; Huang, Q. Numerical study on the summer circulation of the upper South China Sea and its establishment. *Acta Oceanol. Sin.* **2005**, *1*, 31–38.
89. Yanagi, T.; Sachoemar, S.I.; Takao, T.; Fujiwara, S. Seasonal Variation of Stratification in the Gulf of Thailand. *J. Oceanogr.* **2001**, *57*, 461–470. [CrossRef]
90. Qiao, F.; Yang, Y.; Lü, X.; Xia, C.; Chen, X.; Wang, B.; Yuan, Y. Coastal upwelling in the East China Sea in winter. *J. Geophys. Res. Space Phys.* **2006**, *111*, 1–11. [CrossRef]
91. Zweng, M.; Reagan, J.R.; Seidov, D.; Boyer, T.P.; Locarnini, R.A.; Garcia, H.E.; Mishonov, A.V.; Baranova, O.K.; Weathers, K.W.; Paver, C.R.; et al. *World Ocean Atlas 2018 Salinity*; Mishonov, A., Ed.; NOAA Atlas NESDIS 82; National Centers for Environmental Information: Silver Sprin, MA, USA, 2019; Volume 2, 50p.
92. Boyer, T.; Levitus, S.; Garcia, H.; Locarnini, R.A.; Stephens, C.; Antonov, J. Objective analyses of annual, seasonal, and monthly temperature and salinity for the World Ocean on a 0.25° grid. *Int. J. Clim.* **2005**, *25*, 931–945. [CrossRef]
93. JPL. JPL CAP SMAP Sea Surface Salinity Products. Ver. 5.0. [Internet]. PO.DAAC. 2020. Available online: https://podaac.jpl.nasa.gov/announcements/2020-12-11-JPL-SMAP-SSS-CAP-V5.0-Dataset-Release (accessed on 20 August 2021).
94. Fore, A.G.; Yueh, S.H.; Tang, W.; Stiles, B.W.; Hayashi, A.K. Combined Active/Passive Retrievals of Ocean Vector Wind and Sea Surface Salinity With SMAP. *IEEE Trans. Geosci. Remote Sens.* **2016**, *54*, 7396–7404. [CrossRef]
95. Chen, X.; Liu, Z.; Wang, H.; Xu, D.; Wang, L. Significant salinity increase in subsurface waters of the South China Sea during 2016–2017. *Acta Oceanol. Sin.* **2019**, *38*, 51–61. [CrossRef]
96. Wyrtki, K. Scientific Results of Marine Investigations of the South China Sea and the Gulf of Thailand 1959–1961. In *Naga Report*; Scripps Institute of Oceanography: La Jolla, CA, USA, 1961; Volume 2, p. 195.
97. Zhang, X.; Sun, C.; Liu, C.; Zhang, L.; Shao, C.; Zhang, X.; Zhao, Y. Evaluation of the Impact of Argo Data on Ocean Reanalysis in the Pacific Region. *Adv. Meteorol.* **2017**, *2017*, 1–12. [CrossRef]
98. Martin, M.; Balmaseda, M.; Bertino, L.; Brasseur, P.; Brassington, G.; Cummings, J.; Fujii, Y.; Lea, D.; Lellouche, J.-M.; Mogensen, K.; et al. Status and future of data assimilation in operational oceanography. *J. Oper. Oceanogr.* **2015**, *8*, s28–s48. [CrossRef]
99. Edwards, C.A.; Moore, A.M.; Hoteit, I.; Cornuelle, B.D. Regional Ocean Data Assimilation. *Annu. Rev. Mar. Sci.* **2015**, *7*, 21–42. [CrossRef] [PubMed]
100. Giddings, S.N.; Fong, D.A.; Monismith, S.G.; Chickadel, C.C.; Edwards, K.A.; Plant, W.J.; Wang, B.; Fringer, O.; Horner-Devine, A.R.; Jessup, A.T. Frontogenesis and Frontal Progression of a Trapping-Generated Estuarine Convergence Front and Its Influence on Mixing and Stratification. *Chesap. Sci.* **2011**, *35*, 665–681. [CrossRef]